Journal of
Instrumentation

Accurate modeling of charge collection properties of small-pitch 3D pixel sensors based on Monte-Carlo simulations

Published by IOP Publishing for Sissa Medialab

Received: *November 13, 2025*
Accepted: *November 20, 2025*
Published: *December 12, 2025*

17th Topical Seminar on Innovative Particle and Radiation Detectors
Siena, Italy
15–19 September 2025

Accurate modeling of charge collection properties of small-pitch 3D pixel sensors based on Monte-Carlo simulations

Jixing Ye[a,b,*] **Marco Bomben**[c] **and Gian-Franco Dalla Betta**[a,b]

[a] *Dipartimento di Ingegneria Industriale, Università degli Studi di Trento, via Sommarive 9, 38123 Trento, Italy*
[b] *Trento Institute for Fundamental Physics and Applications – Istituto Nazionale di Fisica Nucleare (TIFPA-INFN), via Sommarive 14, 38123 Trento, Italy*
[c] *APC, Université Paris Cité, CNRS/IN2P3, 10 rue Alice Domon et Léonie Duquet, 75013 Paris, France*

E-mail: jixing.ye@unitn.it

Abstract: The exceptional radiation hardness of small-pitch 3D pixel sensors has paved the way for their deployment in the innermost layers of both ATLAS and CMS for the High-Luminosity LHC upgrade. Developed using single-sided process, the fabrication technology of this type of sensors is now mature enough to explore smaller feature size layouts targeting 4D tracking applications, such as the VELO2 detector upgrade designed for LHCb. In view of these future upgrades, it is necessary to evaluate the sensors' hit efficiency and timing resolution at pixel-level through the help of TCAD and Monte-Carlo simulations.

A simplified approach based on 2D TCAD simulations is first presented; the results are then coupled with Monte-Carlo simulations to evaluate the in-pixel hit efficiency of the sensor under various operation conditions. Simulation results show a 100% hit efficiency before irradiation even at low reverse bias, which decreases after bulk damage. The results are in good agreement with the efficiencies measured on 3D sensor modules for the ATLAS Inner Tracker upgrade. To better account for the influence of different regions (e.g., the surface and the gap regions between the column tips and the backside), more comprehensive modeling approaches are introduced. They are based on segmenting the sensor into distinct parts to reduce the computational load of TCAD simulations. The corresponding maps are then extended and stitched together for subsequent simulations. These approaches have a more realistic approximation of the sensor structure and allow assessment of the efficiency in the gap region as well as the influence of surface damage.

Keywords: Detector modelling and simulations II (electric fields, charge transport, multiplication and induction, pulse formation, electron emission, etc); Hybrid detectors; Particle tracking detectors; Solid state detectors

*Corresponding author.

https://doi.org/10.1088/1748-0221/20/12/C12017

2025 JINST 20 C12017

Contents

1 Introduction

Different from planar sensors which house the electrodes on the surfaces of the substrate, 3D sensors feature vertical electrodes that penetrate deep into the silicon bulk [1]. This configuration decouples the inter-electrode distance from the wafer thickness, thereby enabling ultra-radiation-hard performance without compromising the sensor thickness [2]. To exploit this advantage for High Energy Physics (HEP) experiments such as the Large Hadron Collider (LHC), the R&D of 3D sensors has undergone extensive development since their first proposal in the 1990s [3]. Among these, 3D Double-side Double Type Column (3D-DDTC) pixel sensors fabricated by Fondazione Bruno Kessler (FBK) and Instituto de Microelectrónica de Barcelona (IMB-CNM) represent a key benchmark through their integration into part of the ATLAS Insertable B-Layer (IBL) [4–6]. The sensors were deployed in the IBL during the first long shutdown in 2013 and have been operating for over a decade, with experimental results demonstrating their exceptional radiation-hardness characteristics [7].

To boost the discovery of new physics, the LHC will undergo a systematic upgrade in the coming years, and enter its High-Luminosity phase (HL-LHC). Compared with the current LHC, the HL-LHC will have a significantly higher event pile-up (~ 200 per bunch-crossing) and is expected to reach a fluence on the order of 1×10^{16} 1 MeV n_{eq} cm^{-2} in the innermost tracking layer [8, 9]. Encouraged by the excellent performance of 3D-DDTC sensors, small-pitch 3D pixel sensors with different layouts have been developed to cope with the foreseen harsh radiation environment, i.e., 25×100 µm^2 and 50×50 µm^2, each with one readout electrode (referred to as 25×100-1E and 50×50-1E, respectively) [10]. Comprehensive irradiation and beam test campaigns on small-pitch 3D pixel sensors in recent years have demonstrated that these devices can achieve the target hit efficiency after the expected fluence [11–13], leading to the decision to equip the first layer of the ATLAS barrel region with 25×100-1E sensors, and the endcap region with 50×50-1E sensors. Besides that,

2025 JINST 20 C12017

25×100-1E sensors will populate the first layer of the CMS barrel region, marking another important milestone in the 3D sensor technology.

In addition to their excellent radiation hardness, 3D sensors are intrinsically fast, making them strong candidates for 4D tracking applications that require ultra-radiation-hard performance. Furthermore, with stepper lithography now in use [14], the technology at FBK is mature enough to support designs optimized for timing with smaller pixel sizes and additional electrodes, as proposed in [15]. Moreover, it has been shown that, by replacing cylindrical electrodes with trenches, 3D sensors can reach a timing resolution of ∼10 ps after a fluence of 1×10^{17} 1 MeV n_{eq} cm^{-2} [16, 17].

As 3D sensors show tremendous potential for future HEP applications, establishing a full-chain simulation workflow is essential to understand both their electrical and functional characteristics. Such a workflow is also important for interpreting experimental results and guiding optimization. Although several works have been carried out to simulate the electrical characteristics of the sensors and the transient behavior of critical regions within them [18, 19], studies evaluating their functional performance at the pixel-level remain scarce. Apart from limited work on the charge collection efficiency (CCE) and transient response [20, 21], there have been no investigations exploring pixel-level performance of 3D sensors after irradiation. To this end, the present work focuses on simulating sensor performance both before and after irradiation by combining TCAD and Monte-Carlo simulations. As a case study, the simulation domain uses a 50×50-1E sensor, but the proposed approaches can be readily extended to different sensor geometries.

The paper is organized as follows: section 2 focuses on the device under study and simulation platforms; section 3 introduces the simplified approach to evaluate the hit efficiency of 50×50-1E on pixel-level, results are compared with measurements; different methods are presented in section 4 to enable a more precise modeling of the structure; followed by conclusions in section 5.

2 Simulation platforms

2.1 Device description

Compared to 3D-DDTC, small-pitch 3D pixel sensors use much thinner active layers (∼150 µm), which allows a significant reduction in the electrode size and pixel dimensions that would otherwise be limited by the aspect ratio. Compared to their predecessor installed in the IBL of ATLAS, the diameter of the electrodes is reduced from 12 µm to 5 µm, and the overall pixel size is 5 times smaller. To achieve this scaling without worrying about wafer bowing, the high-resistivity sensor wafer is bonded to a highly p-doped support wafer, as shown in figure 1 (left).

The fabrication is based on single-sided technology; all the electrodes are etched from the front side of the wafer using Deep Reactive Ion Etching (DRIE) technology. The ohmic electrodes are made passing through the bulk into the support wafer for direct reverse bias from the back, whereas a gap between the junction electrodes and the backside is present to avoid early breakdown. As indicated in the figure, this configuration divides the sensor into two different regions: the core region and the gap region.

Other features such as different passivation layers, poly-Si caps on both types of electrodes, and the contact opening are visible in the plot as well. FBK continued the tradition of using uniform p-spray to isolate the n^+ readout electrodes, as this does not require additional masks. Figure 1 (right)

2025 JINST 20 C12017

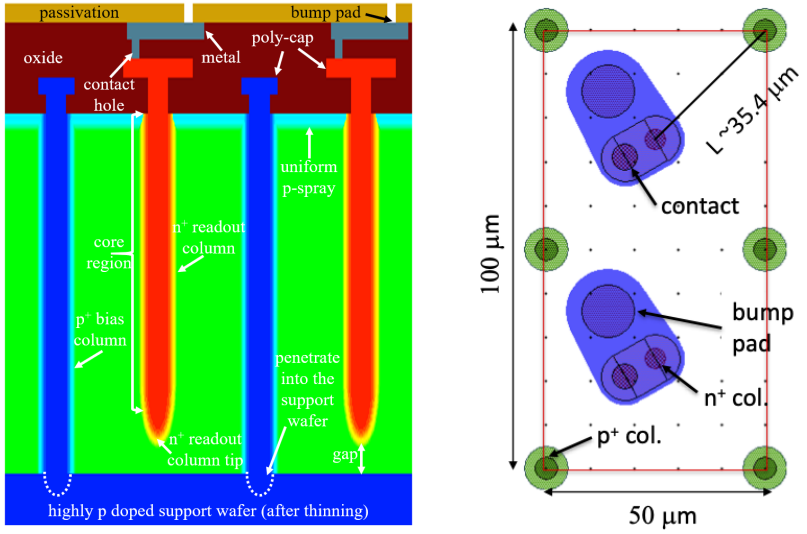

Figure 1. Schematic of small-pitch 3D pixel sensors (left) and layout of 50×50-1E geometry (right).

shows the layout of 50×50-1E with two adjacent pixel cells, where the positioning of different elements (e.g., the electrodes, the contact metal, etc) is apparent.

2.2 TCAD simulations

3D TCAD simulations incorporating parameters that reflect the fabrication process, such as the doping profile of the electrodes, isolation layer, and geometries of different regions in the sensor, can predict the electrical properties of the device with high accuracy. However, this come with the price of time budget, and a trade-off between the mesh size and simulation time often has to be made. The Monte-Carlo simulation platform Allpix^2, on the other hand, relies on uniform mesh to accelerate the simulation [22, 23]. Therefore, it is necessary to have mesh sizes suitable for a smooth transition from adaptive meshing adopted by TCAD to uniform meshing in Allpix^2.

However, 3D TCAD simulation with a small enough global mesh size that covers the entire sensor thickness is infeasible. Since charges generated in the core region are dominated by lateral drift, the TCAD simulation can be simplified into a 2D problem by using a small section of the core region, as shown in figure 2. This simplified approach makes it possible to evaluate different conditions (e.g., reverse bias and fluence) with a fine mesh over the entire sensor, as will be discussed in detail in section 3.

TCAD simulations are performed using Synopsys Sentaurus [24]; typical models, such as doping dependent Shockley-Read-Hall generation/recombination and mobility, high field saturation, are included. To take into consideration of bulk damage effects, the LHCb model is adopted with the highest fluence evaluated being 1.8×10^{16} 1 MeV n_{eq} cm^{-2} [25]. The temperature is set to -31°C, a value within the validation range of the model.

2.3 Monte-Carlo simulation

AllPix^2 is a powerful simulation framework able to simulate charge transportation in the sensor and the digitization process in the front-end electronics. It uses Geant4 for the estimation of energy deposition in the active volume [26]. Electric field and weighting potential maps calculated from TCAD simulations are imported for the calculation of charge propagation and induced signal, respectively [27].

2025 JINST 20 C12017

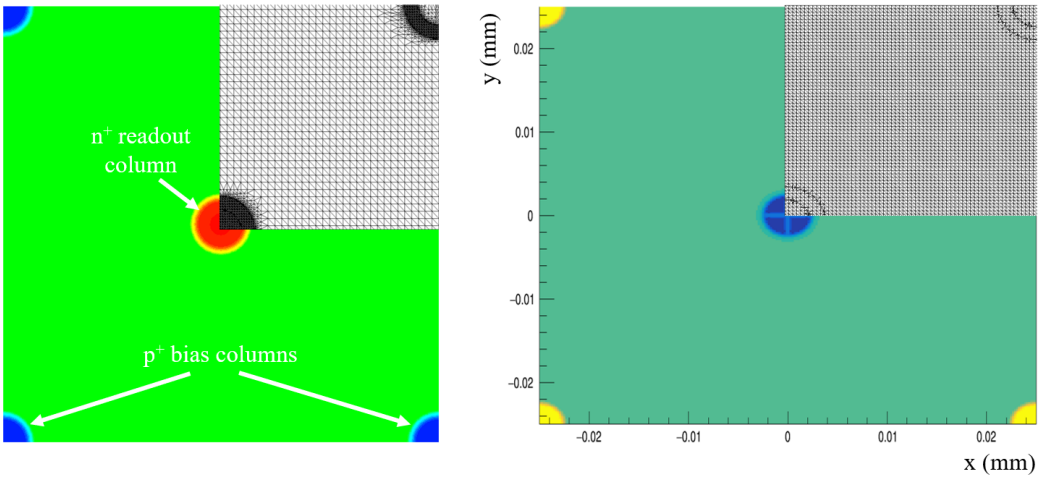

Figure 2. Simulation domain of 50×50-1E in TCAD with adaptive mesh (left) and uniform mesh in Allpix^2 (right) (the gridded areas represent the regions for transient simulations in Allpix^2).

Dedicated front-end electronics can be emulated and used for signal digitization by providing associated parameters such as the feedback capacitance and rise time constant.

Thanks to the symmetric layout, simulating a quarter of the pixel is sufficient to get a full picture of the device's performance (see also figure 2). Hence, all the simulations are performed by scanning minimal ionizing particles (MIP) over the top-right section of the sensor to save time. The MIPs are made perpendicular to the sensor with a scanning step size of 0.25 µm, corresponding to 10,000 events in total. The Jacoboni-Canali model is used for the propagation of the charges [28]; charge trapping after bulk damage is modeled by the effective trapping time described in [29]. The DefaultDigitizer is used for digitizing the signal, with the threshold set to 1000 e^-.

3 A simplified approach

3.1 Field maps

N^+ readout columns penetrate deep inside the bulk as P^+ ohmic columns do, so charges generated along most part of the MIP's track are dominated by lateral drift. The simplified approach fully exploits this advantage, and uses 2D TCAD simulations to acquire the necessary maps for Allpix^2. Figure 3 shows the weighting potential of the central pixel (the region in the red square) in a 3×3 array. As can be seen, the profile of the weighting potential extends into adjacent pixels only, and the array is large enough to account for all the charge sharing in neighboring pixels.

Two different fluences are used in the simulation, i.e., 1.6×10^{16} 1 MeV n_{eq} cm^{-2} and 1.8×10^{16} 1 MeV n_{eq} cm^{-2} to match the irradiation conditions of real devices. Figure 4 shows the respective electric field distribution of the sensor at 100 V before irradiation (top left), after a fluence of 1.6×10^{16} 1 MeV n_{eq} cm^{-2} (top right) and 1.8×10^{16} 1 MeV n_{eq} cm^{-2} (bottom left), respectively; all the electric field profiles along diagonal cuts are shown on the bottom right. It is apparent that low electric field regions exist in the center of all edges and propagate toward the pixel center. Before irradiation, most of the region in the sensor has significant electric field, leading to efficient charge collection. However, the total area that has low electric field increases after bulk damage, despite that

2025 JINST 20 C12017

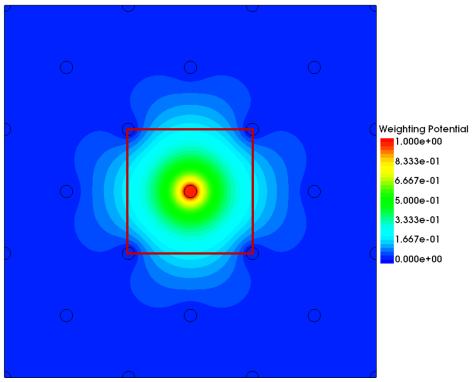

Figure 3. Weighting potential calculated from 50×50-1E with a 3×3 pixel array.

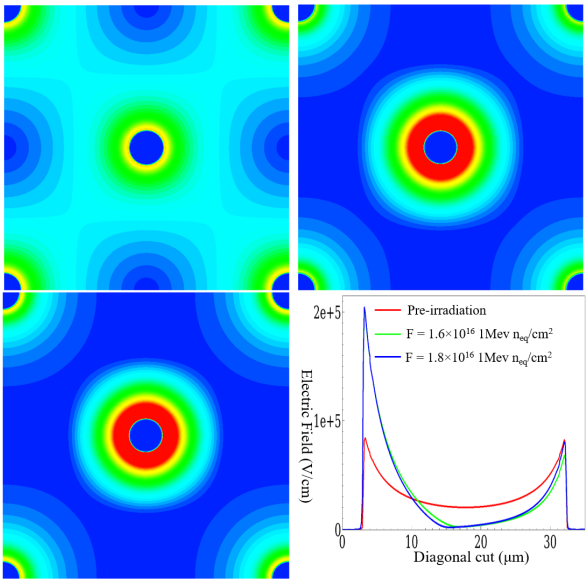

Figure 4. Electric field of 50×50-1E at $V_b = 100\,V$ before irradiation (top left), after a fluence of 1.6×10^{16} 1 MeV $n_{eq}\,cm^{-2}$ (top right), 1.8×10^{16} 1 MeV $n_{eq}\,cm^{-2}$ (bottom left), and the corresponding profile along the diagonal cut (bottom right).

higher peak electric field can be observed near the readout column. It can be seen that the low field areas grow as the fluence increases, subjecting the sensor to severe charge trapping.

3.2 Hit efficiency

In order for the simplified approach to work, we updated part of the Allpix^2 code so as to directly generate 3D maps with any given thickness from 2D TCAD simulation results, i.e., the doping profile, electric field, and weighting potential. To well represent the real sensor, all the conversion are done by setting the thickness to 150 µm. Figure 5 shows the in-pixel hit efficiency map with a fluence of 1.6×10^{16} 1 MeV $n_{eq}\,cm^{-2}$ and 1.8×10^{16} 1 MeV $n_{eq}\,cm^{-2}$ under different reverse biases. All the yellow regions correspond to hits recorded, whereas the dark blue regions didn't register any hits. It is worth mentioning that before irradiation all the MIPs can be recorded even with bias voltage as low as 10 V, except for the columns (i.e., electrodes).

2025 JINST 20 C12017

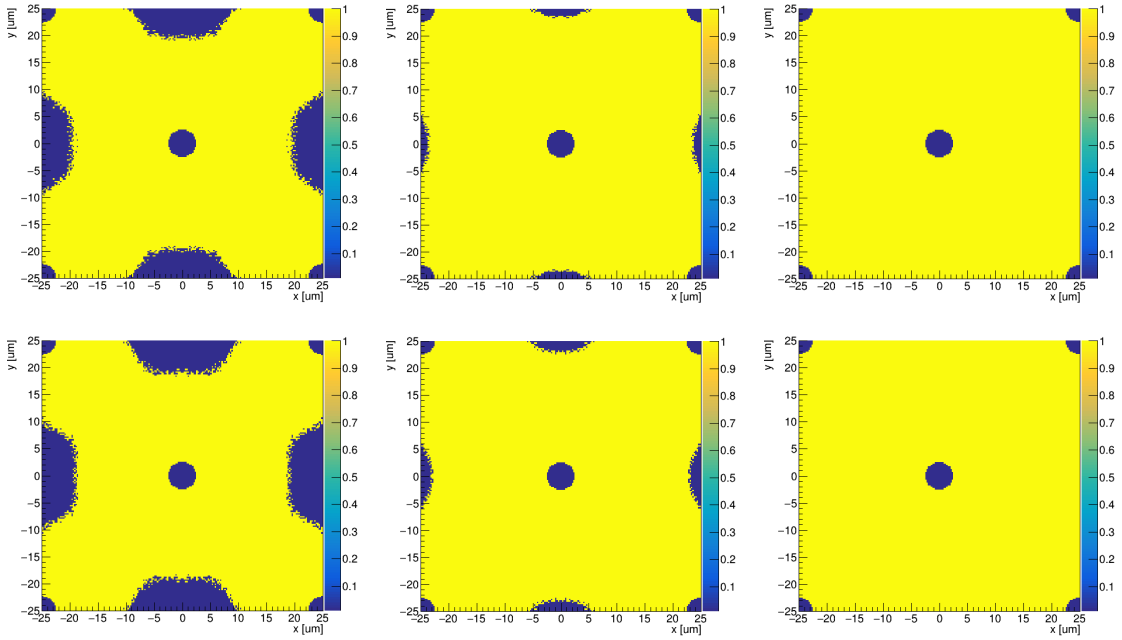

Figure 5. Hit efficiency map after a fluence of 1.6×10^{16} 1 MeV n_{eq} cm^{-2} (top) and 1.8×10^{16} 1 MeV n_{eq} cm^{-2} (bottom). From left to right, the reverse biases applied are 60 V, 100 V, and 140 V, respectively.

Even though the simulations considered only the top-right quarter, the entire hit map is reconstructed by mirroring. It can be seen from the plots that non-responsive regions exist in the sensor after a fluence of 1.6×10^{16} 1 MeV n_{eq} cm^{-2}. The electric field in these regions is low with a bias smaller than ~100 V, charges generated are prone to charge trapping effect which compromises the CCE. On the bright side, the regions shrink as the reverse bias increases, until full efficiency at relatively high voltages. The size of the region grows as the fluence increases, as a consequence, higher voltages are needed to achieve the same performance. Nonetheless, the shape of the simulated hit maps well represents what have been measured on real modules in beam tests.

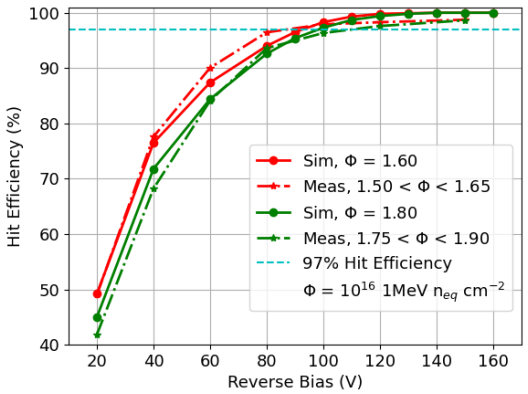

Figure 6. In-pixel hit efficiency under different reverse biases. Measurement data fitted from [30].

Figure 6 reports the simulated hit efficiency in comparison with beam test results. The solid curves show the hit efficiencies from Monte-Carlo simulations, defined as the ratio between the hits recorded in the central pixel of the 3×3 pixel array and the total number of MIPs that do not cross the electrodes,

2025 JINST 20 C12017

for different bias voltages; the dashed curves represent test-beam results from FBK sensors [30]. Both simulations and measurements show that the hit efficiency increases rapidly at low bias voltages, after which it saturates. Although the hit efficiency is higher at a fluence of 1.6×10^{16} 1 MeV n_{eq} cm^{-2}, sensors irradiated to 1.8×10^{16} 1 MeV n_{eq} cm^{-2} can still surpass the 97% hit efficiency requirement set for inclined tracks. Most importantly, despite the fact that the simplified approach does not fully describe the sensor structure and that the LHCb model has not been validated at such high fluences, the simulated hit efficiencies are in good agreement with the experimental results.

4 A more comprehensive approach

4.1 Influence of the gap region

The junction electrodes that are kept at a safe distance from the backside inevitably lead to distorted electric field in the gap region. To account for this effect in the Monte-Carlo simulations, the gap region must be reconstructed in the TCAD simulation. Instead of simulating the full sensor thickness, a compromise can be made by including a section of the core region together with the entire gap region, as shown in figure 7 (left). In this way, it becomes possible to balance the mesh density between critical regions, such as the tip of the junction electrode and the bulk, without overloading the TCAD simulation. A set of Python-based scripts has been developed to extend the converted TCAD simulation results to the full sensor thickness, with the extension starting from the interface of the core region. For example, figure 7 (right) shows the resulting electric field after extension, where the distinct profiles in the gap and core regions are preserved.

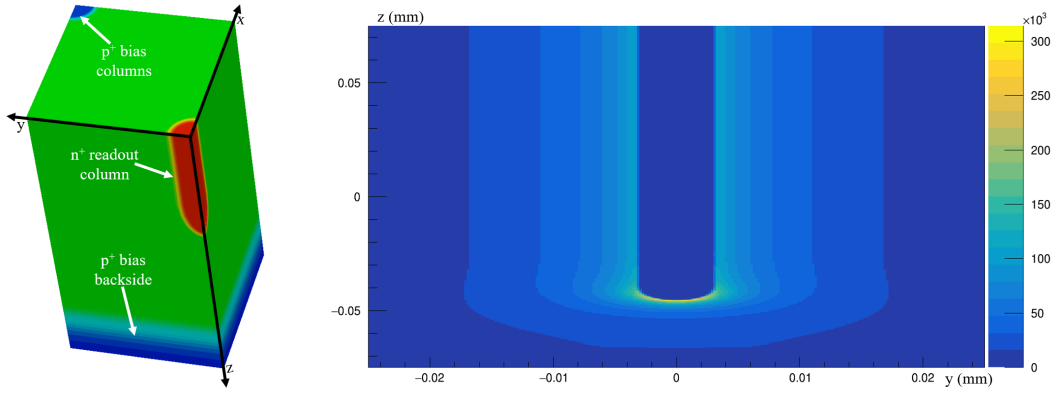

Figure 7. TCAD simulation domain of the gap region (left) and the final electric field profile after conversion (right).

Figure 8 shows the hit maps after irradiation to fluences of 1.6×10^{16} 1 MeV n_{eq} cm^{-2} (top) and 1.8×10^{16} 1 MeV n_{eq} cm^{-2} (right) at different reverse biases. Similarly, regions with no recorded MIP hits originate at the centers of the sensor edges and extend toward the ohmic electrodes and the pixel center. Moreover, the total area of these no-hit regions is larger than that observed with the simplified approach. This can be attributed to several factors. First, the simplified method represents a best-case scenario with a uniform charge collection pattern along the bulk depth, which tends to overestimate the hit efficiency, as the gap region with lower charge collection efficiency is neglected. Second, the back diffusion of dopants from the support wafer extends into the bulk,

2025 JINST 20 C12017

making it more difficult to fully deplete this part of the sensor. However, with this more sophisticated approach, it is possible to evaluate the hit efficiency in the region between the backside and the n^+ readout column tips. As shown in the plots, most of this region already registers hits at 60 V and becomes fully efficient at higher bias voltages.

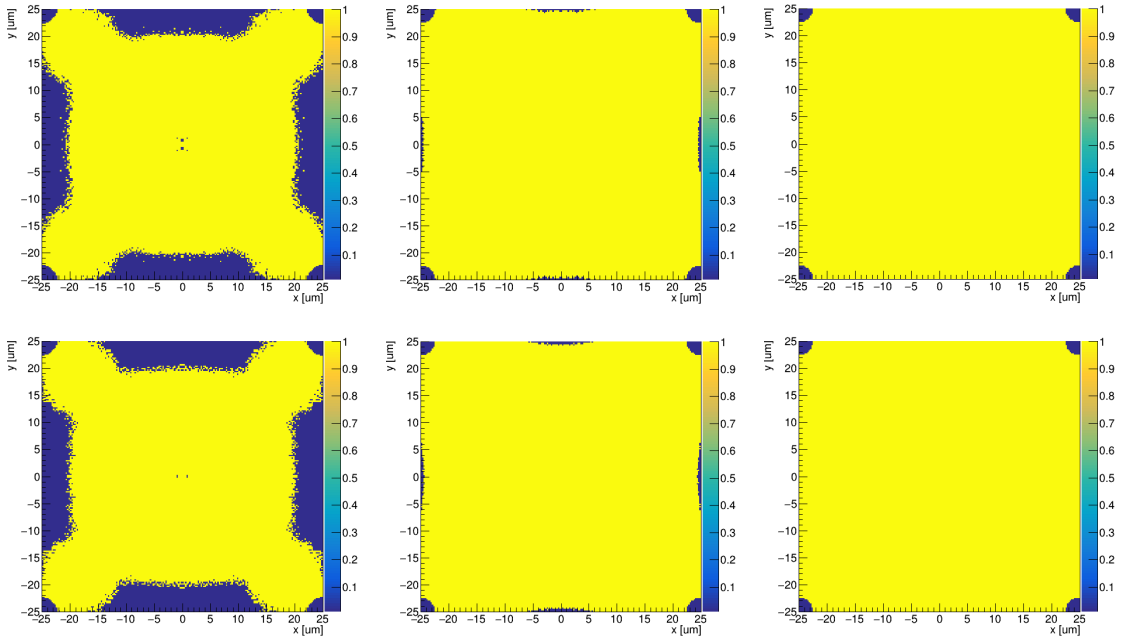

Figure 8. Hit map after a fluence of 1.6×10^{16} 1 MeV n_{eq} cm^{-2} (top) and 1.8×10^{16} 1 MeV n_{eq} cm^{-2} (bottom). From left to right, the reverse biases applied are 60 V, 100 V, and 140 V, respectively.

4.2 Influence of the surface region

Apart from the gap region, the p-spray isolation and radiation induced surface damage also affect the electric field distribution near the surface. To account for these effects, the TCAD simulation can be performed by dividing the sensor into two regions: the surface region, shown in figure 9 (left), and the gap region described in the previous subsection. Specifically, the surface region includes the p-spray isolation, the passivation layer (not shown) for evaluating the total ionizing dose (TID) effect using the Perugia surface damage model [31], and part of the core region. Afterwards, the maps from the gap region are first extended and then stitched to the maps from the surface region. Figure 9 (right) illustrates the resulting electric field distribution obtained using this methodology. A high electric field can be observed at both the surface junction and the tip of the readout electrode.

Simulations using this comprehensive approach have been performed to acquire the hit map, with results showing slightly higher hit efficiency. The reason can be attributed to the fact that the poly caps on top the electrodes that act as field plates and TID effect helps in depleting the surface area and they collectively have a positive effect on charge collection process near it. Above all, this method allows a full evaluation of the sensor's performance, and can be extended to other structures which the surface plays a more important role.

2025 JINST 20 C12017

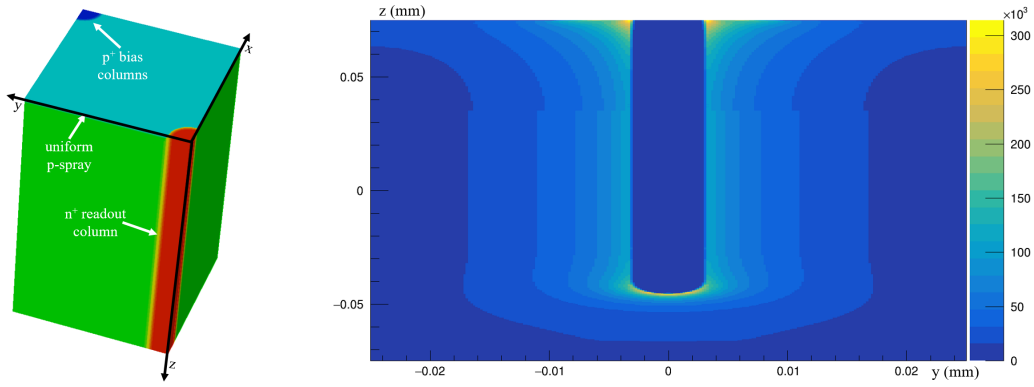

Figure 9. TCAD simulation domain of the surface region (left) and the final electric field profile after conversion (right).

5 Conclusion

Thanks to their outstanding radiation hardness, 3D sensors have gained increasing attention in the HEP community. Decades of R&D has led to remarkable achievements, such as 3D-DDTC installed in the ATLAS IBL and small-pitch 3D pixel sensors to be deployed in the innermost tracking layers of ATLAS and CMS for the High Luminosity LHC upgrade. Beyond these milestones, there are extensive ongoing efforts aiming to further push their limits toward 4D tracking under even higher fluences. Despite these exciting developments, there is still a lack of a full-chain simulation workflow capable of evaluating the in-pixel performance of different 3D sensors, which would be valuable for future upgrade designs. To this end, the present work introduces different methodologies that enable the evaluation of sensor performance at pixel-level.

A simplified approach has been proposed that uses 2D TCAD simulations to get the necessary results. The corresponding maps are extended before being loaded into Allpix^2. Simulation results show that the hit map has the same pattern with what have been reconstructed from test beam on real modules, and the in-pixel hit efficiencies are in good agreement with test beam measurements for devices irradiated up to 1.8×10^{16} 1 MeV n_{eq} cm^{-2}.

More comprehensive methods have also been explored to study the influence of the surface, including the isolation layer and TID effect, as well as the gap region. These methods are based on dividing the sensor into different parts to enable a fine global mesh while reducing the computational load of TCAD simulations. The resulting maps from the different parts are then extended and stitched together for subsequent Monte-Carlo simulations. Results show that the more comprehensive approaches lead to slightly lower hit efficiencies due to the fact that it is harder to full deplete the gap region especially after bulk damage. However, these approaches makes it possible to consider combined radiation damage effects and evaluate the efficiency of the gap region, and they can be extended to other 3D-structured sensors.

Acknowledgments

The authors acknowledge funding from INFN-CSN5 with Project TIMESPOT, and the European Union's Horizon 2020 Research and Innovation programme under GA no. 101004761. The authors would also like to thank Simon Spannagel (DESY, Hamburg, Germany), Håkan Wennlöf (Nikhef, Amsterdam, The Netherlands), and Matteo Polo (University of Trento and TIFPA INFN, Trento, Italy) for fruitful discussions.

2025 JINST 20 C12017

References

[1] S.I. Parker, C.J. Kenney and J. Segal, *3-D: A new architecture for solid state radiation detectors*, *Nucl. Instrum. Meth. A* **395** (1997) 328.

[2] C. Da Vià, G.-F. Dalla Betta and S. Parker, *Radiation sensors with 3D electrodes*, CRC Press (2019) [DOI:10.1201/9780429055324].

[3] G.-F. Dalla Betta and M. Povoli, *Progress in 3D Silicon Radiation Detectors*, *Front. in Phys.* **10** (2022) 927690.

[4] G. Giacomini et al., *Development of Double-Sided Full-Passing-Column 3D Sensors at FBK*, *IEEE Trans. Nucl. Sci.* **60** (2013) 2357.

[5] G. Pellegrini et al., *3D double sided detector fabrication at IMB-CNM*, *Nucl. Instrum. Meth. A* **699** (2013) 27.

[6] C. Da Vià et al., *3D silicon sensors: Design, large area production and quality assurance for the ATLAS IBL pixel detector upgrade*, *Nucl. Instrum. Meth. A* **694** (2012) 321.

[7] ATLAS collaboration, *Sensor response and radiation damage effects for 3D pixels in the ATLAS IBL Detector*, 2024 *JINST* **19** P10008 [arXiv:2407.05716].

[8] ATLAS collaboration, *Technical Design Report for the ATLAS Inner Tracker Strip Detector*, CERN-LHCC-2017-005 (2017).

[9] I. Béjar Alonso et al., *High-Luminosity Large Hadron Collider (HL-LHC): Technical design report*, CERN-2020-010 (2020) [DOI:10.23731/CYRM-2020-0010].

[10] G.-F. Dalla Betta et al., *Development of a new generation of 3D pixel sensors for HL-LHC*, *Nucl. Instrum. Meth. A* **824** (2016) 386 [arXiv:1612.00624].

[11] M. Meschini et al., *Radiation resistant innovative 3D pixel sensors for the CMS upgrade at the High Luminosity LHC*, *Nucl. Instrum. Meth. A* **978** (2020) 164429.

[12] M.A.A. Samy et al., *Characterization of FBK 3D pixel sensor modules based on RD53A readout chip for the ATLAS ITk*, 2021 *JINST* **16** C12028.

[13] S. Terzo et al., *Novel 3D Pixel Sensors for the Upgrade of the ATLAS Inner Tracker*, *Front. Phys.* **9** (2021) 624668.

[14] M. Boscardin et al., *Advances in 3D Sensor Technology by Using Stepper Lithography*, *Front. Phys.* **8** (2021) 625275.

[15] A. Loi, A. Lai, J. Ye and G.-F. Dalla Betta, *Timing-Optimised 3D Silicon Sensor with Columnar Electrode Geometry*, *Sensors* **25** (2025) 926.

[16] F. Borgato et al., *Charged-particle timing with 10 ps accuracy using TimeSPOT 3D trench-type silicon pixels*, *Front. Phys.* **11** (2023) 1117575.

[17] M. Addison et al., *Characterisation of 3D trench silicon pixel sensors irradiated at* 1×10^{17} *1 MeV* n_{eq} cm^{-2}, *Front. Phys.* **12** (2024) 1497267.

[18] D.M.S. Sultan et al., *First Production of New Thin 3D Sensors for HL-LHC at FBK*, 2017 *JINST* **12** C01022 [arXiv:1612.00638].

[19] J. Ye, A. Loi, A. Lai and G.-F. Dalla Betta, *Design and simulation of modified 3D-trench electrode sensors*, 2023 *JINST* **18** C11021.

[20] G.T. Forcolin et al., *Development of 3D trenched-electrode pixel sensors with improved timing performance*, 2019 *JINST* **14** C07011.

2025 JINST 20 C12017

[21] A. Loi, A. Contu and A. Lai, *Timing Optimisation and Analysis in the Design of 3D silicon sensors: the TCoDe Simulator*, 2021 *JINST* **16** P02011 [arXiv:2008.10730].

[22] S. Spannagel et al., *Allpix^2: A Modular Simulation Framework for Silicon Detectors*, *Nucl. Instrum. Meth. A* **901** (2018) 164 [arXiv:1806.05813].

[23] S. Spannagel and P. Schütze, *Allpix^2 — silicon detector Monte Carlo simulations for particle physics and beyond*, 2022 *JINST* **17** C09024 [arXiv:2112.08642].

[24] Synopsys Inc., *Sentaurus Device User Guide Version R-2020.09*, San Jose, CA, U.S.A. (2020).

[25] Å. Folkestäd et al., *Development of a silicon bulk radiation damage model for Sentaurus TCAD*, *Nucl. Instrum. Meth. A* **874** (2017) 94.

[26] J. Allison et al., *Recent developments in Geant4*, *Nucl. Instrum. Meth. A* **835** (2016) 186.

[27] W. Shockley, *Currents to Conductors Induced by a Moving Point Charge*, *J. Appl. Phys.* **9** (1938) 635.

[28] C. Jacoboni, C. Canali, G. Ottaviani and A. Alberigi Quaranta, *A review of some charge transport properties of silicon*, *Solid State Electron.* **20** (1977) 77.

[29] I. Mandić et al., *Measurements with silicon detectors at extreme neutron fluences*, 2020 *JINST* **15** P11018 [*Erratum ibid.* **16** (2021) E03001] [arXiv:2007.05418].

[30] G. Calderini et al., *Qualification of the first pre-production 3D FBK sensors with ITkPixV1 readout chip*, *PoS* **Pixel2022** (2023) 025.

[31] A. Morozzi, F. Moscatelli, T. Croci and D. Passeri, *TCAD Modeling of Surface Radiation Damage Effects: A State-Of-The-Art Review*, *Front. Phys.* **9** (2021) 617322.

2025 JINST 20 C12017